Macromolecules

Subscriber access provided by COMISION NAC DE ENERGIA ATOMICA

Article

Coarse-Grained Description of a Brush#Melt Interface in Equilibrium and under Flow

C. Pastorino, K. Binder, and M. Mu#ller

Macromolecules, **2009**, 42 (1), 401-410• DOI: 10.1021/ma8015757 • Publication Date (Web): 10 December 2008

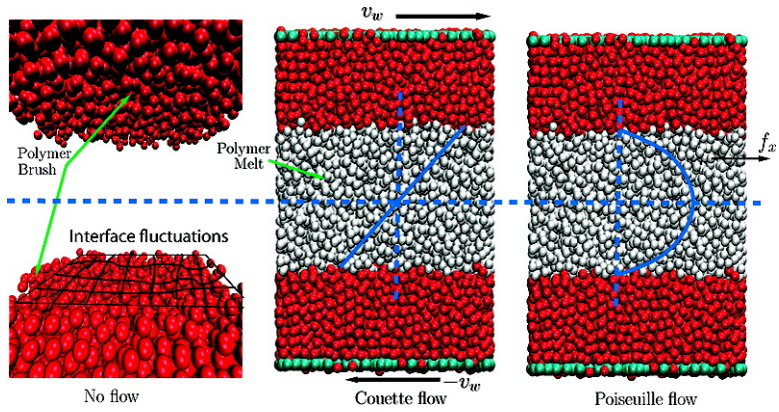

More About This Article

Additional resources and features associated with this article are available within the HTML version:

- Supporting Information
- Access to high resolution figures
- Links to articles and content related to this article
- Copyright permission to reproduce figures and/or text from this article

View the Full Text HTML

Coarse-Grained Description of a Brush−Melt Interface in Equilibrium and under Flow

C. Pastorino,*,†,§ K. Binder,‡ and M. Müller‡,§

Departamento de Fisica, Centro Atomico Constituyentes, CNEA-CONICET, Av. Gral. Paz 1499, 1650 Pcia. de Buenos Aires, Argentina; Institut für Physik WA331, Johannes Gutenberg-Universität, 55099 Mainz, Germany; and Institut für Theoretische Physik, Georg-August-Universität, Friedrich-Hund-Platz 1, 37077 Göttingen, Germany

Received July 12, 2008; Revised Manuscript Received November 14, 2008

ABSTRACT: The equilibrium and flow properties of a polymer liquid confined in a brush-coated channel are studied by molecular dynamics simulations using a dissipative particle dynamics (DPD) thermostat. We focus on the regime of high-grafting density, where the brush progressively becomes a stiff and smooth, soft surface and layering of the polymer melt at the brush−melt interface is observed. We use the Gibbs criterion to localize the brush−melt interface and analyze its equilibrium fluctuation in terms of a capillary wave Hamiltonian augmented by an elastic term that accounts for the deformability of the brush. Poiseuille and Couette flows are investigated, and the slip length and location of the hydrodynamic boundary are computed. In the high-grafting regime, the brush roughness decreases and slippage is observed. The results are compared to the effective channel width, which is defined via the integrated flow rate for Poiseuille flow. Evidence of local changes of the near-surface viscosity is provided, and the consistency of the Navier slip boundary condition is investigated.

I. Introduction

The properties of fluids at the nanoliter scale have attracted abiding interest for fundamental and applied research.[1,2] Because of the large area-to-volume ratio, the properties of the confining boundaries influence the flow behavior. Commonly, the effect of surfaces enters the macroscopic hydrodynamic description via the Navier−Stokes equation as boundary condition. This hydrodynamic boundary condition encodes the molecular structure and dynamics at the surface by a few parameters (e.g., slip length[3] and boundary position). It is independent from the type and strength of flow, but it is a material property of the surface. The interplay between the equilibrium structure at the interface, the flow at the surface, and the concomitant boundary condition, however, is only incompletely understood.

Much effort has been directed toward tailoring surface properties. Molecular simulations are well suited to investigate how changes of the molecular conformations at surfaces, adsorption layers, or coatings influence the surface free energy and stress. This information enters into the macroscopic description in form of a boundary condition. Thus, computing the parameters of the boundary condition via molecular simulation is a first step toward a multiscale modeling of microfluidic devices from the molecular structure to the length scale of micrometers.

Much of the equilibrium behavior on large length scales is dictated by the surface free energy. For instance, the contact angle of a droplet on a surface is given by Young's equation,[4] which describes the balance of the surface and interface tensions at the three-phase contact line. Similarly, the dynamic properties are often described in terms of a balance between viscous and friction stress of the flow at the surface. In the Navier slip condition, this balance is used to define the slip length.[3]

In this paper, the flow of a polymer liquid over a dense brush comprised of identical polymers is studied by molecular dynamics simulations of a coarse-grained polymer model.[5] Polymer brushes are a stable and robust surface coating with potentially useful properties such as a pronounced reduction of friction,[6] which is useful for increasing the flow at a fixed pressure difference, or nonspecific protein adsorption, which can be exploited to avoid clogging of microfluidic channels. The properties of polymer brushes in an explicit solvent of homopolymers[7−12] as well as the flow of polymers over hard surfaces[13−19] have previously been studied by simulations. Here, we simultaneously investigate the equilibrium position of the brush−melt interface, its fluctuations, and the liquid flow in its vicinity and explore to what extent the different static and dynamic estimates of the position of the soft, fluctuating interface coincide.

The properties of the brush−melt interface can be altered by the grafting density.[20−24] Already this deceptively simple system exhibits a rich wetting behavior as a function of grafting density encompassing both first- and second-order wetting transitions as well as autophobicity.[9,22,25,26] This autophobic regime between polymer brushes or networks and chemically identical chains has been experimentally observed.[27−29] The equilibrium behavior of this soft, deformable surface is dictated by the interdigitation between brush and melt. Since these properties stem from the rather universal aspects of the conformational entropy of long, flexible molecules in a dense melt and are not dominated by enthalpic interactions of the constituents, this problem is particularly well suited for coarse-grained modeling.

Our paper is arranged as follows: In the next section, we discuss the coarse-grained description of the brush−melt interface in equilibrium and under flow. Then, we use molecular simulations of a coarse-grained model to determine the parameters of the coarse-grained description: the position and tension of the brush−melt interface, its coupling to the solid substrate, and the slip length. In particular, different measures of the location of the brush−melt interface are studied as a function of the grafting density. The paper closes with a brief summary and concluding remarks.

II. Model and Simulation Details

We used a coarse-grained bead−spring model[5] of polymers, which has been applied to a variety of thermodynamic conditions and physical regimes such as dilute solutions, melts, and

* To whom correspondence should be addressed.
† CNEA-CONICET.
‡ Johannes Gutenberg-Universität.
§ Georg-August-Universität.

10.1021/ma8015757 CCC: $40.75
Published on Web 12/10/2008

glasses.[7,25,30−32] The interaction between neighboring beads along the same polymer is modeled by a finitely extensible nonlinear elastic (FENE) potential:

$$U_{\mathrm{FENE}} = \begin{cases} -\frac{1}{2}kR_0^2 \ln\left[1 - \left(\frac{r_{ij}}{R_0}\right)^2\right] & \text{for } r_{ij} \le R_0 \\ \infty & \text{for } r_{ij} > R_0 \end{cases} \quad (1)$$

where the maximum allowed bond length is $R_0 = 1.5\sigma$, the spring constant is $k = 30\varepsilon/\sigma^2$, and $r_{ij} = |\mathbf{r}_i - \mathbf{r}_j|$ denotes the distance between neighboring monomers. Excluded volume interactions at short distances and van der Waals attractions between segments are described by a truncated and shifted Lennard-Jones (LJ) potential:

$$U(r) = U_{\mathrm{LJ}}(r) - U_{\mathrm{LJ}}(r_c) \quad (2)$$

with

$$U_{\mathrm{LJ}}(r) = 4\varepsilon\left[\left(\frac{\sigma}{r}\right)^{12} - \left(\frac{\sigma}{r}\right)^{6}\right] \quad (3)$$

where the LJ parameters, ε and σ, define the units of energy and length, respectively. Temperature is given in units of ε/k_B, with k_B being the Boltzmann constant. $U_{\mathrm{LJ}}(r_c)$ is the LJ potential evaluated at the cutoff radius. We work in the regime of poor solvent conditions, in which the LJ cutoff is twice the minimum of the LJ potential, $r_c = 2 \times 2^{1/6}\sigma$. Under these conditions, the effective attraction among monomers are included giving rise to liquid−vapor phase separation[33,34] and droplet formation[16,35] below the Θ-temperature, $\Theta = 3.3\varepsilon/k_B$. The bare substrate is modeled as an ideally flat and impenetrable wall, which interacts with the polymer segments via an integrated Lennard-Jones potential:

$$V_{\mathrm{wall}}(z) = |A_w|\left(\frac{\sigma_w}{z}\right)^9 - A_w\left(\frac{\sigma_w}{z}\right)^3 \quad (4)$$

where $A_w = 3.2\varepsilon$ and $\sigma_w = 1\sigma$ are sufficient to make the liquid wet the bare substrate.[25,34,36]

In the following, we consider short chains comprised of $N = 10$ monomers. The equilibrium properties at temperature $k_BT/\varepsilon = 1.68$ have been previously studied.[36] The density of the melt, which coexists with a vapor of vanishingly low density, is $\rho_m = 0.61\sigma^{-3}$ and the end-to-end distance of the polymers is $R_e = \sqrt{\langle R_e^2\rangle} = 3.66\sigma$. This corresponds to an invariant degree of polymerization, $\mathcal{N} \equiv (\rho R_e^3/N)^2 = 8.94$. Brush molecules are tethered with an end bead at a distance of 1.2σ from the wall. Their lateral position is randomly chosen and immobile. The grafting density, ρ_g, denotes the number of grafted brush chains per unit surface area. The simulations at different grafting densities are performed at constant channel widths, $D_w = 30\sigma$ ($\rho_g^* \equiv \rho_g R_e^2 = 0.80$, 5.89, 10.31) and $D_w = 40\sigma$ for higher values of grafting density ($\rho_g^* = 13.40$, 17.95, 27.06, 35.10, and 43.80). In some simulations, $D_w = 50\sigma$ has been utilized with a smaller sample in $\hat{y}$: $L_y = 9.09\sigma$. The surface area of the simulation cell is $L_x \times L_y = 21.00\sigma \times 18.19\sigma$. As the grafting density increases and the brush height, $\rho_g^*/\sqrt{\mathcal{N}}$ grows, the melt region shrinks for constant distance D_w between walls.

We use a DPD thermostat[37,38] to maintain constant temperature across the channel in equilibrium and under flow. The dissipative and frictional forces are applied in a pairwise form, such that the sum of thermostatting forces acting on a particle pair equals zero. The forces are given by

$$\mathbf{F}_i^{\mathrm{D}} = \sum_{j(\neq i)} \mathbf{F}_{ij}^{\mathrm{D}}; \quad \mathbf{F}_{ij}^{\mathrm{D}} = -\gamma\omega^{\mathrm{D}}(r_{ij})(\hat{\mathbf{r}}_{ij}\cdot\mathbf{v}_{ij})\hat{\mathbf{r}}_{ij} \quad (5)$$

$$\mathbf{F}_i^{\mathrm{R}} = \sum_{j(\neq i)} \mathbf{F}_{ij}^{\mathrm{R}}; \quad \mathbf{F}_{ij}^{\mathrm{R}} = \sigma\omega^{\mathrm{R}}(r_{ij})\theta_{ij}\hat{\mathbf{r}}_{ij} \quad (6)$$

where for each vector, $\mathbf{a}$, we define $\mathbf{a}_{ij} \equiv \mathbf{a}_i - \mathbf{a}_j$, γ is the friction constant, and σ characterizes the noise strength. Friction and noise obey the relation $\sigma^2 = 2k_BT\gamma$, and the fluctuation−dissipation theorem will be satisfied if[39]

$$[\omega^{\mathrm{R}}]^2 = \omega^{\mathrm{D}} \quad (7)$$

θ_{ij} is a random variable with zero mean and second moment:

$$\langle\theta_{ij}(t)\theta_{kl}(t')\rangle = (\delta_{ik}\delta_{jl} + \delta_{il}\delta_{jk})\delta(t - t') \quad (8)$$

We use the standard weight functions

$$[\omega^{\mathrm{R}}]^2 = \omega^{\mathrm{D}} = \begin{cases} (1 - r/r_c)^2 & r < r_c \\ 0 & r \ge r_c \end{cases} \quad (9)$$

where r_c is the cutoff radius. Alternatively, one could choose a different set of functions, obeying eq 7, to improve the efficiency of the thermostat. This may be important for nonequilibrium simulations.[40]

The Hamiltonian equations of motion[41,42] for monomer i take the form

$$\dot{\mathbf{r}}_i = \frac{\mathbf{p}_i}{m_i}$$
$$\dot{\mathbf{p}}_i = \mathbf{F}_i + \mathbf{F}_w + \mathbf{F}_i^{\mathrm{D}} + \mathbf{F}_i^{\mathrm{R}} \quad (10)$$

where $\mathbf{F}_i$ is the total conservative force on each particle, obtained from the gradient of the LJ and FENE potentials, and m_i is the mass of each monomer. $\mathbf{F}_w$ is the force on the particle exerted by the wall. We set $m_i = 1$ in the following. $\mathbf{F}_i^{\mathrm{D}}$ and $\mathbf{F}_i^{\mathrm{R}}$ are the forces due to the DPD thermostat according to eq 5 and 6, respectively. The equations of motion (10) are integrated using the velocity Verlet algorithm[41,42] with a time step of $dt = 0.002\tau$, where $\tau = \sigma(m/\varepsilon)^{1/2}$ denotes the LJ time unit. The grafted beads of the brush chains interact with other beads with LJ and FENE potentials, but its positions are held fixed during the simulation. The LJ potential among grafted beads is not taken into account.

The short chains obey Rouse-like dynamics with a diffusion coefficient, $D = 0.05\sigma^2/\tau$. This defines the longest single-chain relaxation time, $\tau^* = R_e^2/D = 268\tau$. Couette flow was imposed by moving the walls at constant velocity, v_w, in opposite directions,[11] which gives rise to an average shear rate, $\dot{\gamma} = 2v_w/D_w$. We quantify the shear by the Weissenberg number $\mathrm{Wi} = \dot{\gamma}\tau^*/2$. For a typical condition, $v_w = 1\sigma/\tau$ and $D_w = 40\sigma$, we obtain $\mathrm{Wi} = 6.7$.

Additionally, we study Poiseuille flow by adding a constant body force, f_x, for each monomer (except the immobile grafting points) in the direction parallel to the walls.

III. A Coarse-Grained Description of the Brush-Coated Surface

Molecular dynamics simulation provides detailed information about the structure and its spatial dependence at the solid substrate and the brush−melt interface. Descriptions of the large scale properties, like wettability or flow, do not regard the subtle packing effects and profiles of orientations of the extended molecules at the surface, but they rather describe these molecular details in form of coarse-grained parameters. For the equilibrium properties, one routinely utilizes an effective interface Hamiltonian that describes the system in terms of the interface position, the interface tension, and the free energy it takes to place the brush−melt interface at a position z, the interface potential $g(z)$. For flow properties, one describes the interface

by the position of the hydrodynamic boundary and the slip length. In the following, we will compute and compare the equilibrium and dynamic parameters that enter a coarse-grained description of the deformable, brush-coated surface.

A. Coarse-Grained Description of Equilibrium Properties. The equilibrium properties of the brush−melt interface can be described by an effective interface Hamiltonian, $\mathscr{H}_{cap}$, which is commonly used to discuss interface fluctuations and wetting properties. Rather than describing the details of the molecular conformations, we utilize a description in terms of the local interface position, $z_G(x, y)$. z_G describes the local distance of the brush−melt interface from the solid substrate, and it depends on the two lateral coordinates, x and y. The effective interface Hamiltonian[43]

$$\mathscr{H}_{cap}[z_G(x,y)] = \int d^2(x,y)\left(\frac{\sigma_{int}}{2}[\nabla z_G]^2 + g(z_G)\right) \quad (11)$$

is comprised of two terms. The first one describes the free energy costs of the excess area that is created by interface fluctuations or capillary waves. It is proportional to the interface tension, σ_{int}, of the brush−melt interface. The second term describes the coupling of the interface and the solid substrate. Interface fluctuations deform the polymer brush, and the concomitant free energy costs strongly suppress long wavelength fluctuations. In the following we assume that the interface potential can be expanded around the equilibrium brush height, $\bar{z}_G$, and takes the form

$$g(z_G) = \frac{k}{2}(z_G - \bar{z}_G)^2 \quad (12)$$

The free energy penalty of a surface deformation of molten brushes has been considered within the strong stretching approximation. These calculations typically consider an incompressible brush and a sharp brush−melt interface. Under these conditions, there are no fluctuations with large wavelength, i.e., $k \sim 1/q^2$.[44−46] In our simulations, however, the brush is compressible (but the equation of state of the Lennard-Jones fluid is not quantitatively describable by a second-order virial expansion). Thus, a spatially homogeneous displacement of the brush−melt interface (with $q = 0$) is possible. To obtain an order of magnitude estimate of the free energy change associated with a homogeneous motion of the brush−melt interface, we assume that each chain acts like an entropic spring, i.e., $k \sim \rho_g k_B T/R_e^2$.

Different schemes to locate the interface position have been devised;[47] here we use a simple integral criterion. To this end, we subdivide the simulation cell into a square grid of columns with lateral extensions Δ_x and Δ_y, which span the simulation cell in z-direction.[48] Typically, we use $\Delta_x = \Delta_y = 1\sigma$ such that there are 20 × 20 columns. In each column, characterized by (x, y), we compute $z_G(x, y)$ as the location of the Gibbs dividing surface. To minimize the effect of bulklike density fluctuations far away from the interface, the integral criterion is only applied to a narrow interval $[z_-:z_+]$ around z_G. As illustrated in Figure 1, $z_G(x, y)$ is chosen such that

$$\int_{z_-}^{z_+} dz\, \rho_{x,y}(z) = (z_+ - z_G(x,y))\rho_m^{bulk} \quad (13)$$

where $\rho_{x,y}(z)$ denotes the segment density of melt chains in a column and ρ_m^{bulk} is the density at the center of the channel.

The choice of the width of the interval $[z_-,z_+]$ is a compromise. On the one hand, it should be large enough to bracket the fluctuations of the interface. On the other hand, it should be small enough to minimize the effect of bulklike

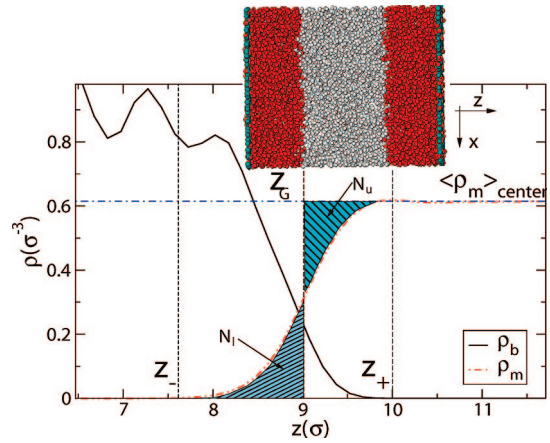

Figure 1. Profiles of the segment density of brush and free chains (melt) for $\rho_g^* = 10.31$. A sketch of the quantities defined for the calculation of the Gibbs dividing surface $Z_G(x,y)$ is shown. The shaded areas N_u and N_l are the geometrical regions that must be equated to determine the position $Z_G(x,y;t)$ of the interface. Inset: snapshot of the simulated system. Liquid monomers are shown in light gray and brush monomers in dark gray. The position, z_G, agrees with the main panel, but the z-scale is much reduced. The coordinate system is indicated with arrows; $\hat{x}$ defines the flow direction.

density fluctuations far away from the interface. The effect of bulklike fluctuations on interface fluctuations and their coupling have been the subject of much debate.[47,49−55] To estimate the effect of the interval width, we assume that bulk and interface fluctuations decouple. Then, the additional fluctuations due to bulklike density fluctuations are of the order $\langle \delta z_G^2 \rangle_{bulk} \propto \kappa_T k_B T |z_+ - z_-|/[2\Delta_x\Delta_y]$ where $\kappa_T \approx 1\sigma^3/\varepsilon$ denotes the isothermal compressibility. Since bulklike density fluctuations are uncorrelated on lengths larger than the microscopic scale set by the screening length ξ, their effect on large length scales is significantly smaller. Thus, different methods of computing the local interface position differ in the large-q behavior; however, they yield identical results in the limit of $q \to 0$. Therefore, we believe that our observation $k \to$ const instead of $k \sim q^{-2}$ is not related to the specific technique by which we compute the interface position.

It is useful to discuss the behavior as a function of the lateral wavevector, $\mathbf{q} = (q_x, q_y)$, that characterizes the deformation of the brush−melt interface; i.e., one considers a deformation of the form[34,48,56,57]

$$z_G(x,y) = \frac{c_c(0)}{2} + \sum_{q_x,q_y} c_c(\mathbf{q})\cos(q_x x + q_y y) + \sum_{q_x,q_y} c_s(\mathbf{q})\sin(q_x x + q_y y) \quad (14)$$

Inserting an interface deformation of the form (14) into eq 11, one finds that the different Fourier components decouple and

$$\mathscr{H}_{cap}(c_c(\mathbf{q})) = \frac{L_x L_y}{4}(\sigma_{int}\mathbf{q}^2 + k)c_c(\mathbf{q})^2 \quad (15)$$

Since each mode is independent and quadratic, the equipartition theorem dictates

$$\langle c_c^2(\mathbf{q})\rangle = \frac{2k_B T}{L_x L_y(\sigma_{int}\mathbf{q}^2 + k)} \quad (16)$$

Therefore, the spectrum of fluctuations of the local brush−melt interface position provides information about the tension of the brush−melt interface and its deformability. We will use this

coarse-grained description to analyze our simulation data in section IV.A.2.

In general, the two parameters of the effective interface Hamiltonian, σ_{int} and k, are wavevector-dependent. The q dependence of the interface tension has attracted abiding interest,[47,49−55] and an expansion in terms of even powers of q is commonly assumed. These effects have been observed inter alia at polymer−polymer interfaces and melt−vapor interfaces.[34,56,58] Details at large wavevectors, $q\sigma \sim \mathcal{O}(1)$, may depend on the details of the method by which the local interface position is extracted from the simulation. For this reason we focus on the small q behavior, which is not affected by the details of the algorithm to compute the local interface position.

B. Coarse-Grained Description of Flow Properties. In order to capture the salient features of the brush−melt interface under flow, one has to provide a boundary condition to the hydrodynamic equations that describe the flow on large time and length scales far away from the surface. Commonly, the Navier slip condition is utilized[3]

$$\left.\frac{\partial v_x(z)}{\partial z}\right|_{z_b} = \left.\frac{\lambda}{\eta} v_x(z)\right|_{z_b} \equiv \left.\frac{1}{b} v_x(z)\right|_{z_b} \tag{17}$$

which is based on the equality of frictional stress, $\sigma_{fric} = \lambda v_x(z_b)$, and viscous stress, $\eta \partial v_x/\partial z$, at the surface. λ denotes the friction coefficient, and η is the bulk viscosity of the liquid. This boundary condition is characterized by two parameters: z_b characterizes the position of the hydrodynamic boundary, and $b = \eta/\lambda$ denotes the slip length. Note that for a soft surface—like a brush-coated solid—the position, z_b, at which the boundary condition is to be applied is not obvious, and both parameters have to be computed. If eq 17 serves as a boundary condition for the Navier−Stokes equation, which describes the flow of the liquid far away from the surface, the parameters z_b and b should not depend on the type and strength of the flow, but they are material parameters of the surface.

We will use Couette and Poiseuille flows to determine the parameters of the boundary condition and test its consistency. Couette flow far away from the surface (i.e., at the center of the channel) is described by a linear velocity profile

$$v_{hydro,C}(z) = \dot{\gamma}(z - z_C) \tag{18}$$

where $\dot{\gamma}$ denotes the shear rate and z_C is the position where the linear profile at the center extrapolates to zero. If one drives the flow by a volume force, $g_x = \rho_m^{bulk} f_x$, where f_x denotes the force that acts on each melt segment, one will obtain a parabolic velocity profile

$$v_{hydro,P}(z) = \frac{g_x}{2\eta}(z - z_P)(D_w - z_P - z) \tag{19}$$

at the center of the channel. z_P denotes the location where the velocity profile of Poiseuille flow at the center extrapolates to zero. Using these predictions of the Navier−Stokes equation in eq 17, one obtains[59]

$$b = \sqrt{(z_P - z_C)(D_w - z_P - z_C)} \tag{20}$$

$$z_b = z_C + b \tag{21}$$

A necessary condition for the consistency of the Navier slip condition is $z_P \geq z_C$. The condition $z_P = z_C$ characterizes the limit of no-slip boundary condition, $b = 0$. If $z_P < z_C$, the Navier slip condition will fail to provide a consistent boundary condition to the macroscopic, hydrodynamic description which solely depends on the surface but is independent of the type and strength of the flow.

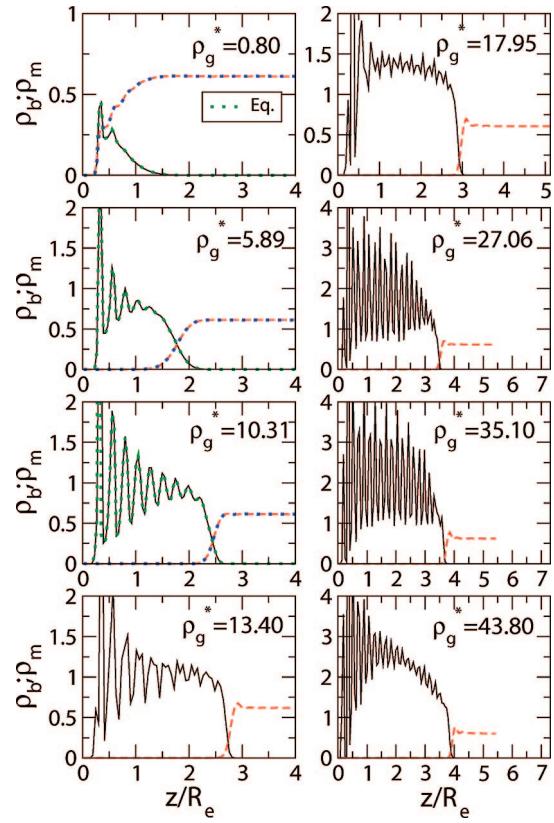

Figure 2. Density profiles of brush and melt for the whole range of grafting densities. Data correspond to Poiseuille flow with a small body force, $f_x = 0.008\varepsilon/\sigma$. For the three lower grafting densities, the equilibrium profiles are presented in dotted lines.

IV. Results

A. Equilibrium Properties. *1. Density Profiles.* The density profiles across the channel are presented in Figure 2 for Poiseuille flow with a small volume force, $f_x = 0.008\varepsilon/\sigma$. Profiles are symmetrized around the center of the channel. The complete range of grafting densities ρ_g is shown—from the mushroom regime ($\rho_g^* = 0.80$) in which the liquid reaches the rigid wall, over the brush regime, for which a brush−melt interface is formed ($\rho_g^* \in [5.89, 10.31]$), up to very high grafting densities, where the brush behaves like an elastic solid surface with a very small interpenetration of the melt. Under these conditions, flow hardly affects the profile of the brush layer.

At low grafting densities, the free chains of the melt penetrate the brush, and there is a broad brush−melt interface.[11] Upon increasing the grafting density, we observe a gradual growth of the layering at the solid substrate. The brush−melt interface becomes thinner, and for the highest grafting densities, the brush gradually approaches the behavior of an attractive solid surface.

The thickness, L_{brush}, of the brush can be quantified by the first moment of the brush density profile, $\rho_b(z)$

$$L_{brush} = 2\frac{\int dz\, z\rho_b(z)}{\int dz\, \rho_b(z)} \tag{22}$$

The factor 2 ensures that in the case of a brush of uniform density and a sharp brush−melt interface, L_{brush} coincides with the position of the brush−melt interface.

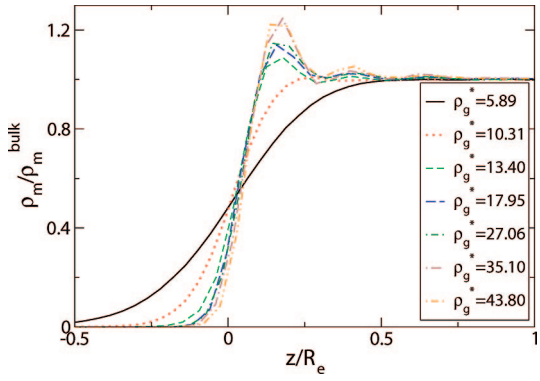

Figure 3. Melt density profiles for different grafting. The density has been adjusted such that its value at the center equals the coexistence density, $\rho_0 \simeq 0.61\sigma^{-3}$. The curves were shifted in z by z_G such that the interface position is located at $z/R_e = 0$ for all the densities. The onset of layering in the melt at very high grafting densities is clearly observed.

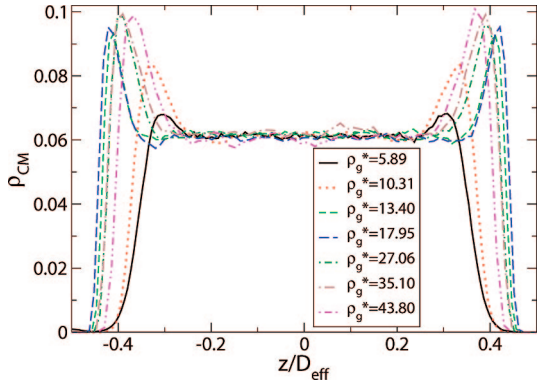

Figure 4. Number density of the center of mass of molecules $\rho_{CM}(z)$ across the channel, normalized with the effective channel width $D_{eff} = D_w - 2z_G$.

We note that the high density inside the brush gives rise to a strong attraction between brush and melt. For the highest values of grafting density, ρ_g^*, it is difficult to equilibrate the brush due to a glassy-like state at such a high densities, but the profiles are stable during the course of the simulation. As shown in Figure 3, oscillations of the melt density signal the layering and ordering in the melt.

The profile $\rho_{CM}(z)$ of the center of mass density, which is presented in Figure 4, also exhibits a gradual increase of layering upon increase of the grafting density.

2. Fluctuations of the Brush−Melt Interface. We analyze the fluctuations of the brush−melt interface by computing the local, instantaneous Gibbs dividing surface on a grid of 20 × 20 points for 3000 up to 24 000 configurations which are separated by 300 MD time steps. We have verified that the interface fluctuations (Figure 5) are sampled over a significant number of uncorrelated configurations beyond the relaxation time of the Fourier mode with the smallest wavevector.

First, we calculated the variance of the local interface positions, $(\langle h^2\rangle)^{1/2} \equiv [\langle (z_G(x,y) - \bar{z}_G)^2\rangle_{x,y;t}]^{1/2}$. This quantity characterizes the roughness of the brush−melt interface on the length scale of the binning size, σ. Figure 5 presents the data for various ρ_g^*. For $\rho_g^* < 5.89$, there is no brush−melt interface and the melt reaches the wall without important influence of the grafted chains. For $\rho_g^* > 6$, we observe a decrease of the roughness in accord with a thinning of the brush−melt interface and a stiffening of the stretched brush.

We have extracted the local, instantaneous interface position, $z_G(x,y)$, and calculated the y-averaged Fourier components, $c_c(q_x)$

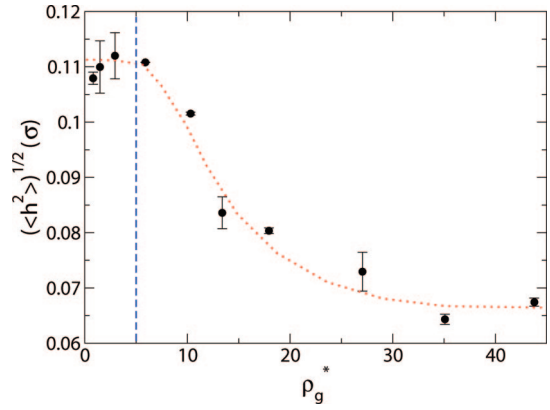

Figure 5. Mean fluctuation of the interface $(\langle h^2\rangle)^{1/2}$ as a function of grafting density. In all the cases, a binning size of $\Delta x = 1\sigma$ has been used. The dotted curve only is a guide for the eye. The vertical dashed line indicates the limit for which the brush−melt interface is completely built up.

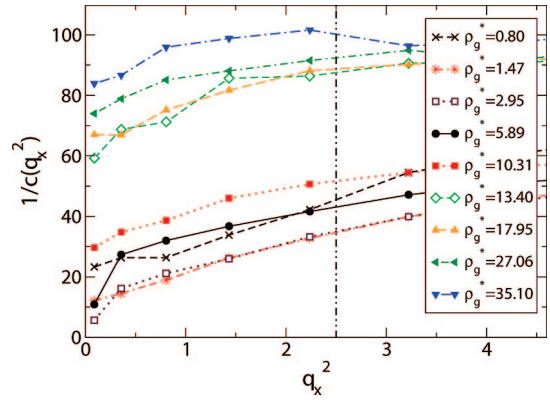

Figure 6. Mean amplitude of the Fourier modes $\langle c(q_x)^2\rangle$ vs q_x^2. From this graph is extracted the interface tension σ_{int} and the elastic constant, k, of the brush layer. Only data to the left of the dashed line have been analyzed, and the curves connecting the data points are guides to the eye only.

$= c_c(q_x, q_y = 0)$. According to eq 16, the curve $1/\langle c(q_x)^2\rangle$ vs q_x^2 should be linear within the interval, in which the effective Hamiltonian description is valid. Figure 6 presents simulation data for a very wide range of grafting densities. For large wavevectors, q_x, the coarse-grained interface description breaks down, and the granularity of the beads and details of the interaction potentials matter. In Figure 6, this limit is marked by a vertical, dashed line, and we have not used the data for larger wavevectors in our analysis. Previous work has shown that the asymptotic limit $q \to 0$ is approached beyond several molecular diameters.[48,60,61] Using the rather large range of the smallest four or five q_x values for the linear fit, we extract the tension of the brush−melt interface, σ_{int}, and the elastic constant, k, of the binding potential.

Figure 7 shows the values of the normalized interface tension, $\sigma_{int}\sigma^2/k_BT$ (top panel), and brush elastic constant, $k\sigma^4/k_BT$ (bottom panel), as a function of grafting density. The vertical line indicates the crossover toward a fully developed brush−melt interface. For smaller values of ρ_g^*, the structure and tension of the "brush−melt" interface resemble the surface of the melt close to the solid substrate. Since the pressure corresponds to the coexistence value, the rise of the density resembles the properties of a liquid−vapor interface whose value is $0.1k_BT/\sigma^2$. On the other hand, k decreases with ρ_g^* because the brush is easier to deform for decreasing grafting densities.

For larger grafting densities, $\rho_g^* > 6$, we observe a slight increase of the σ_{int} which saturates at large ρ_g^* within the rather

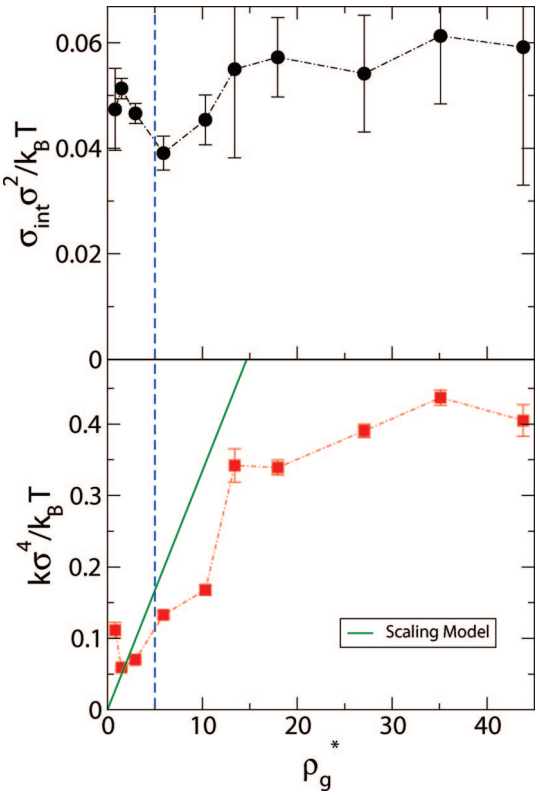

Figure 7. Top: tension of the brush−melt interface, σ_{int}, as a function of grafting density ρ_g^*, as extracted from interface fluctuations. Bottom: elastic constant, k, of the brush as a function of the grafting density. The vertical dashed line indicates the limiting case, in which the brush−melt interface is completely built up. For lower grafting densities, the melt reaches the solid surface, and the interface is not completely developed. The solid line indicates the linear dependence of the scaling model.

large uncertainties of the simulation data. In this regime of grafting densities, the elastic constant k first increases linearly with ρ_g^* and saturates at large ρ_g^*.

To rationalize the linear increase of k for $\rho_g^* \lesssim 15$, we used a simple scaling model. The excess free energy of a stretched chain in the brush can be written as

$$\frac{F_{chain}}{k_BT} \sim \frac{h^2}{Nb^2} + \frac{\upsilon N^2 \rho_g}{2hb^2} \tag{23}$$

where h is the brush height, b the statistical segment length, $b^2 = R_e^2/N$, and υ the segmental volume (or second order virial coefficient). The first term of the right-hand side of eq 23 is the stretching free energy, and the second one accounts for the excluded volume interaction among segments. The equilibrium height h_0 can be found by minimizing eq 23 with respect to h, yielding $h_0 \sim N(\upsilon b^2 \rho_g/4)^{1/3}$.

If we now perform a Taylor expansion around the equilibrium height h_0 up to second order, one obtains

$$\frac{F_{chain}(h)}{k_BT} - \frac{F_{chain}(h_0)}{k_BT} \simeq \frac{3}{Nb^2}(h - h_0)^2 \tag{24}$$

Equation 24 expresses the excess free energy per chain. If we identify the brush height h with the position of the brush melt interface, z_G, one obtains for the interface potential

$$g(z) \simeq \frac{3k_BT\rho_g}{R_e^2}(z - \bar{z}_G)^2 \tag{25}$$

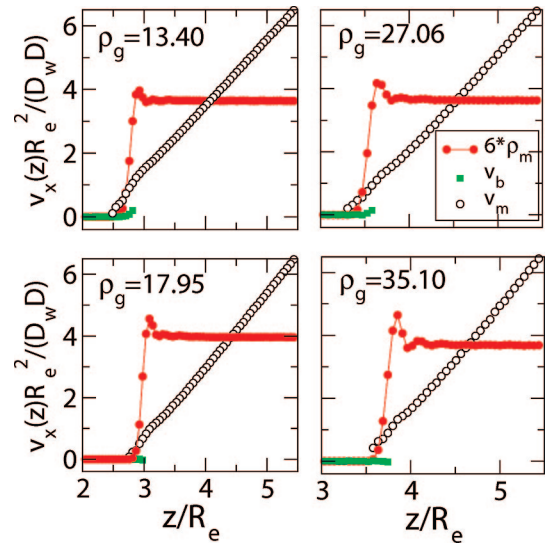

Figure 8. Symmetrized velocity profile for Couette flow. The wall velocity is $1\sigma/\tau$ (Wi = 6.7). The frame reference is set at the wall comoving frame. The melt velocity profile, setting $z/R_e = 0$ at the wall position, is shown in open circles. The brush velocity profile, following the wall velocity ($\upsilon = 0$), is presented in solid squares, and the melt density (scaled by a factor 6) in solid circles and lines. The latter shows the layering in the vicinity of the melt.

i.e., each chain acts like an entropic spring and the elastic constant takes the form $k \simeq (6k_BT\rho_g)/R_e^2 = (6/R_e^4)k_BT\rho_g^*$. This simple scaling consideration rationalizes the linear dependence of k on the grafting density. Using the value $R_e \approx 3.66\sigma$, we depict the prediction by the solid line in Figure 7.

B. Flow Properties. *1. Couette Flow.* Figure 8 presents the symmetrized velocity profile of Couette flow with wall velocity, $\upsilon_w = 1\sigma/\tau$, i.e.,Wi = 6.7. The position, $z = 0$, indicates the wall location, and the coordinate system is defined at the wall comoving frame. The density profiles are also shown to correlate the flow profile with the position of the interface determined in the previous section. At small and intermediate grafting densities, we observe that the velocity of the melt attains the value of the wall.

High grafting density gives rise to a stronger attraction between the brush and melt because the density inside the brush increases in our compressible model, but this effect is more than compensated by the decrease of the roughness of the brush−melt interface. In fact, the melt velocity, at high grafting densities, remains smaller than that of the boundary. This phenomenon we denote by apparent slip. If one *extrapolated* the linear velocity profile of the melt, then the melt would attain the velocity of the wall at some location inside the brush.[11] At that position, however, the melt density is virtually zero.

The velocity profiles for different shear rates are presented in Figure 9. Data for the velocity are omitted for densities smaller than $0.05\rho_m^{bulk}$. Lines indicate the linear velocity profiles and have been fitted to the central region of the channel with a width of $10\sigma \approx 3R_e$. We note that the slope of the velocity profile changes on the melt side of the brush−melt interface. At $\rho^* = 35.1$, the velocity gradient, $\partial v_x/\partial z$, is smaller at the interface than at the center. Assuming that the viscous stress is continuous through the brush−melt interface, this observation indicates an increased local viscosity of the melt in the vicinity of the interface, which is compatible with the increase of the local density.

From the Couette flow profiles, we estimate the position $z_C = z_b - b$, where the linear velocity profile at the center extrapolates to zero. In case of a no-slip boundary condition, z_C will characterize the position at which the hydrodynamic

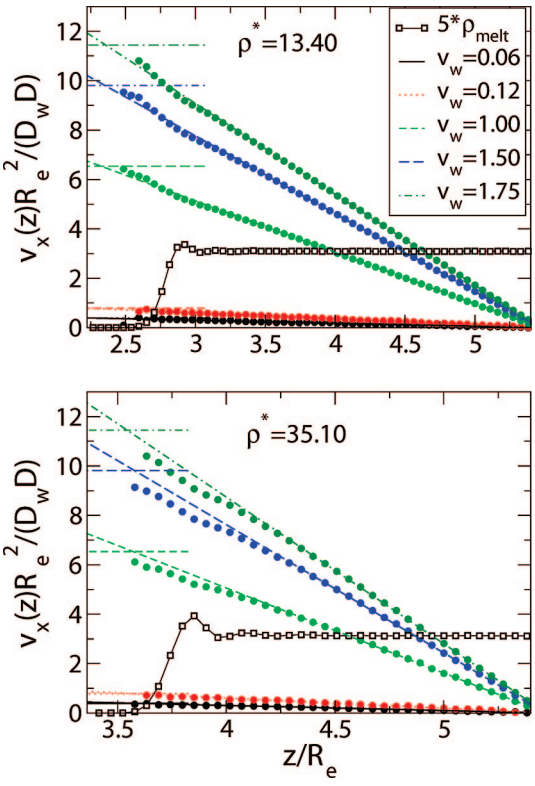

Figure 9. Symmetrized velocity profiles at different shear rates for grafting densities, $\rho_g^* = 13.40$ (top panel) and $\rho_g^* = 35.10$ (bottom panel). $z/R_e = 0$ defines the wall position. The linear fit at the center of the liquid is shown. The horizontal lines indicate the wall velocity, and the melt density is also shown for comparison.

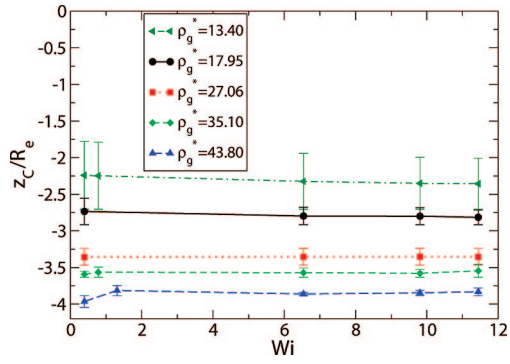

Figure 10. z_C as a function of shear rate at high grafting densities. A negative value indicates that the boundary lays inside the channel (close to the brush−melt interface). z_C as well as the density profile does not strongly depend on shear rate. The dominant effect is the increase of the effective brush thickness for higher grafting densities. Lines are a guide to the eye.

boundary condition is to be applied, i.e., $z_C = z_b$. For the shear rate considered, z_C is largely independent of $\dot{\gamma}$. This observation agrees with the insensitivity of the profiles. Moreover, it has been suggested that if the melt (fluid) and the brush (substrate) can efficiently exchange momentum, slippage will be rather independent from shear rate.[62] This condition is fulfilled in our model.

Figure 11 shows the position z_C, L_{brush}, and z_G for different grafting densities. All these measures increase monotonously with grafting density. For intermediate and high grafting densities, z_G and z_C agree, and for very high grafting densities also L_{brush} approaches the other values. At low grafting densities, however, there are differences: (i) At intermediate and low grafting densities, the brush profile differs from the square well

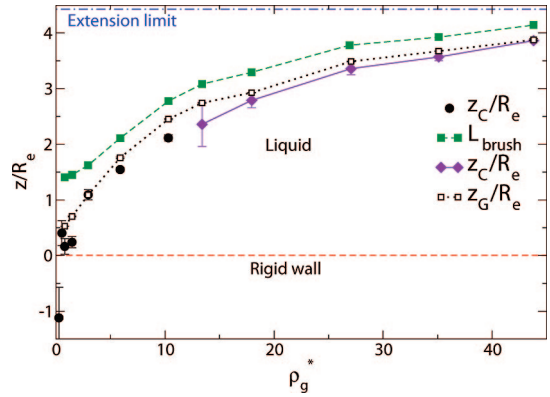

Figure 11. Brush thickness L_{brush} (squares), z_C, and z_G as a function of grafting density. The maximum extension limit of the brush is indicated by the dotted-dashed horizontal line.

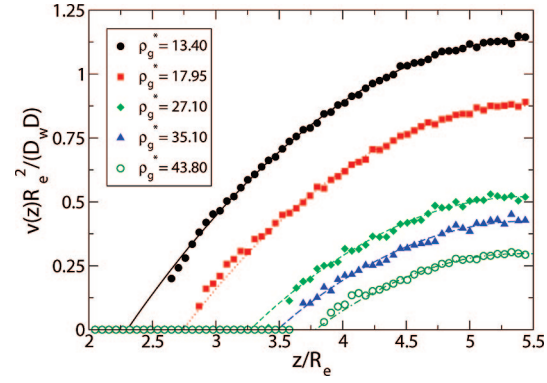

Figure 12. Symmetrized liquid velocity profile for Poiseuille flow simulations as a function of grafting density. The volume force is $f_x = 0.008\varepsilon/\sigma$, and the channel width $D_w = 40\sigma$. The center of the channel is at $z = 20\sigma$ ($z/R_e = 5.46$). The quadratic fit, which corresponds to the solution of Navier−Stokes equation, is also shown. Only data with $15 \le z/\sigma \le 25$ have been used for the parabolic fits.

form, and L_{brush} does not provide a quantitative estimate of the broad brush−melt interface. (ii) At very low grafting densities, the melt slips past the smooth substrate, and z_C adopts negative values.

2. Poiseuille Flow. Applying a constant force to each segment, we generate Poiseuille flow and observe a parabolic velocity profile, $v_x(z)$, at the center. The simulation results for different grafting densities together with parabolic fits to the flow behavior at the center are shown in Figures 12 and 13 for an external force $f_x = 0.008\varepsilon/\sigma$ and channel widths, $D_w = 30\sigma$ and $40\sigma = 10.93R_e$. The interface position is indicated in Figure 13 by dashed lines which present the melt density. Velocity data corresponding to a liquid density below $0.05\rho_m^{bulk}$ are omitted from the graph. In accord with the behavior in shear flow, slippage is observed at very low grafting densities, and apparent slip occurs at very high grafting densities.

As we increase the grafting density, the central region occupied by the melt becomes narrower and the overall flow velocity decreases. From parabolic fits to the hydrodynamic behavior at the center, we extract the position, z_P, and the curvature of the velocity profile at the center (see eq 19). The latter quantity in conjunction with the known body force can be used to calculate the viscosity of the melt. The results are shown in Figure 14. For all but the largest grafting density, we obtain a value $\eta = 1.86(2)$ (in LJ units), which is consistent with previous simulations[11,16] and indicates that bulklike behavior is observed at the center.

Upon increasing the grafting density, the melt regions narrows and the overall flow rate decreases. The total flow rate

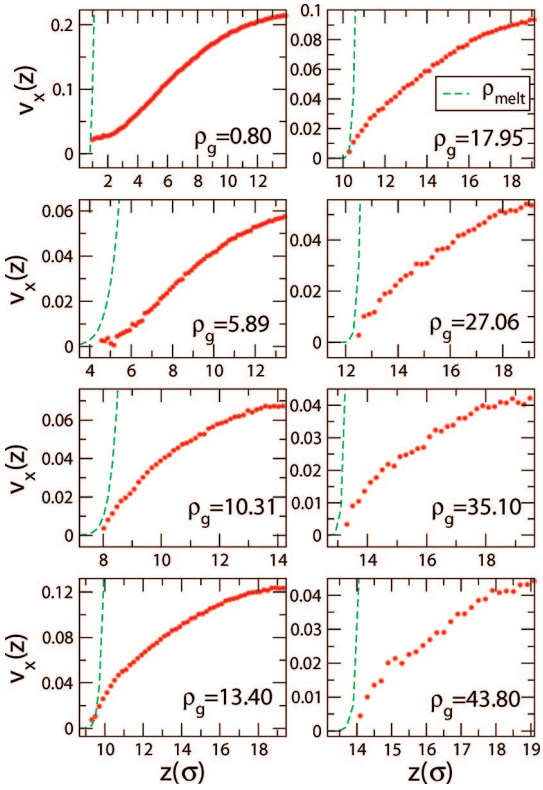

Figure 13. Symmetrized velocity profile (symbols) and density profile for the polymer liquid (dashed line). $T = 1.68\varepsilon/k_B$; $f_x = 0.008\varepsilon/\sigma$. The channel width is $D_w = 30\sigma$ until $\rho_g = 10.31$ and $D_w = 40\sigma$ for larger values of grafting densities. The area of the sample is $A \simeq 20 \times 20\sigma^2$.

$$Q_m = L_y \int_0^{D_w} dz\, \rho_m(z) v_{m,x}(z) \tag{26}$$

is an experimentally accessible quantity. $v_{m,x}$ and ρ_m are the velocity and density of the melt. The inset in Figure 15 shows the profiles $\rho_m(z)v_{m,x}(z)$ for high grafting densities. Assuming a parabolic velocity profile and a no-slip boundary condition, we solve the incompressible Navier−Stokes equation and compute the total flow rate:

$$Q_m^* = L_y \rho_m^{bulk} \frac{f_x}{12\eta} D^3 \tag{27}$$

Comparing the measured flow rate to the prediction, we define an effective channel width,[12] $D_{eff} = [(Q_m/L_y)(12\eta/\rho_m^{bulk} f_x)]^{1/3}$, where all quantities have been computed independently.

The effective width, D_{eff}, as a function of the grafting density is shown in Figure 16, which also depicts the channel width extracted from the position, z_G, of the brush−melt interface. Qualitatively, both data agree. The small differences can be traced back to several causes: (i) layering of the melt at the brush−melt interface, (ii) increase of density and viscosity at the interface, and (iii) apparent slip at very high grafting densities.

3. Hydrodynamic Boundary Condition. Given the apparent slip at very low and very high grafting densities and the ambiguities of defining the position of the soft brush−melt interface, we also utilized the two types of flow to extract the slip length and the position of the hydrodynamic boundary simultaneously.

First, we note that the necessary condition, $z_P > z_C$, for the parameters, b and z_b, of the Navier slip condition to be material parameters of the surface is not fulfilled at intermediate grafting densities, as shown in Figure 17. The difference $z_P - z_C$ is small

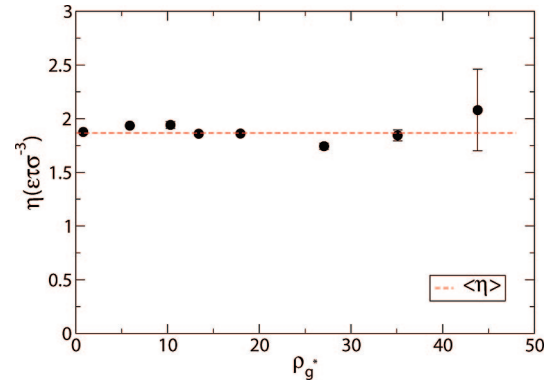

Figure 14. Viscosity estimated from Poiseuille flow with body force $f_x = 0.008\varepsilon/\sigma$ as a function of the grafting density.

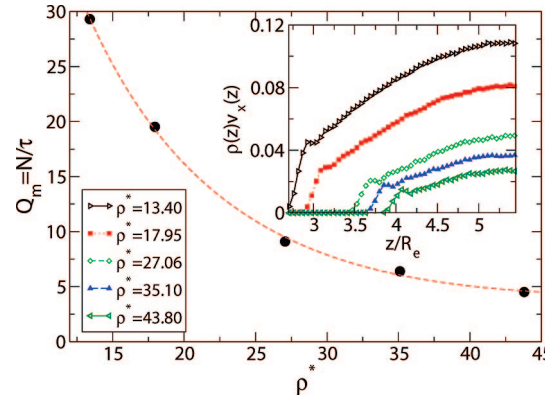

Figure 15. Flow rate for Poiseuille flow in the high grafting interval. The dashed line is a guide for the eyes The inset shows the symmetrized profile $\rho(z)v_x(z)$ for all the grafting densities. The center of the channel is in the origin of coordinates $z/R_e = 0$.

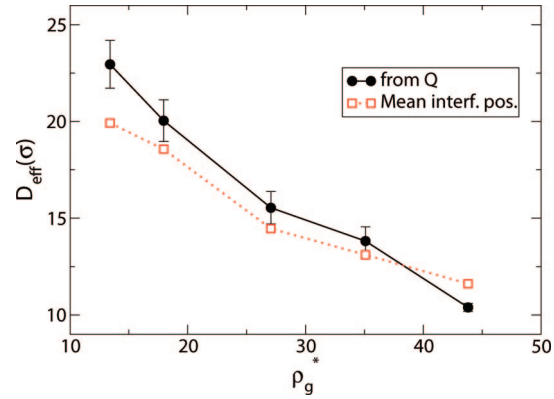

Figure 16. Effective channel width extracted from flow rate (full circles) and using the mean position of the Gibbs dividing surface (open squares) for the high grafting density interval. Lines are a guide to the eye.

but negative, and a similar behavior has also been observed in dynamic single-chain-in-mean-field simulations.[59] This is highlighted in the inset of Figure 17. The failure of the Navier slip condition at intermediate grafting densities can be traced back to an increased viscosity of the melt at the surface compared to the bulk. This is plausible because at intermediate grafting densities the brush chains dangle into the melt and increase the friction, and the velocity of the melt reaches the surface velocity (i.e., microscopically there is no apparent slippage). The local increase of viscosity at the brush−melt interface was already observed in simulations of brushes exposed to monomeric solvents.[63] The failure of the Navier slip condition indicates

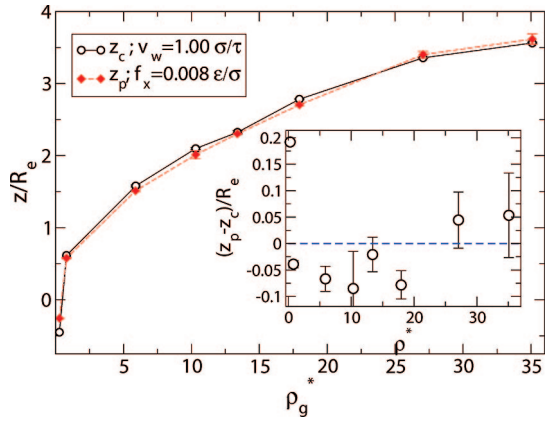

Figure 17. Comparison of z_P and z_C for Poiseuille (diamonds) and Couette (open circles) flows as a function of the grafting density. Inset: difference $z_P - z_C$ for the complete grafting density interval. $z_P - z_C > 0$ indicate the points for which the Navier boundary condition is valid. Even with large error bars, there is a range at intermediate grafting in which the Navier boundary condition is not fulfilled.

Table 1. Slip Length, b, and Interface Position, z_b, for Grafting Densities Which Fulfill the Condition $z_P > z_C$

ρ_g^*	$b(\sigma)$	$z_b(\sigma)$
0.28	4.79(4)	3.1(4)
27.1	1.5(6)	13.9(6)
35.1	1.6(8)	14.7(8)

that changes of liquid structure close to the boundaries are important and cannot be consistently parametrized by the two parameters of the hydrodynamic boundary condition.[17] At very high grafting densities, however, the brush−melt interface becomes very narrow. There is an increased melt velocity at the brush−melt interface because the liquid density is increased compared to the bulk due to the attraction between brush and melt (see Figure 9). This effect is, however, counterbalanced by the apparent slippage at the brush melt interface, which is observed in Figure 9; i.e., the velocity of the melt does nowhere reach the wall velocity. This apparent microscopic slippage is sufficient to restore the Navier slip condition.[17]

Second, for very small grafting densities, $\rho^* = 0.28$, we observe slippage. The position of the hydrodynamic boundary, z_b, is close to the solid grafting surface, and the slip length is quite large, $b = 4.8\sigma$. In the opposite limit of very high grafting densities, we also observe slippage. The slip lengths, b, are much smaller and on the order of a bead diameter. The position, at which the hydrodynamic boundary condition is to be applied, coincides with the brush−melt interface. For this high grafting, the extrapolation of the velocity profiles at the center deviate from the near-surface data as highlighted in Figure 18 for $\rho_g^* = 35.10$, in which z_C an z_P together with the position of the interface z_b are explicitely indicated. The simulation results are compiled in Table 1.

V. Concluding Remarks

In this work, we performed molecular dynamics simulations using a DPD thermostat to study the structure and dynamics of the brush−melt interface in equilibrium and under flow as a function of the grafting density. In analogy to the equilibrium wetting properties,[9,22] three regimes can be identified in the dynamics: (i) At very low grafting densities, the properties of the solid, grafting surface dominate; the smooth substrate used in our study gives rise to slip. (ii) At intermediate grafting density, there is a broad brush−melt interface. We find evidence that this results in an increase of the effective shear viscosity in the vicinity of the brush−melt interface. In this regime, the Navier slip condition fails to serve as a boundary condition to

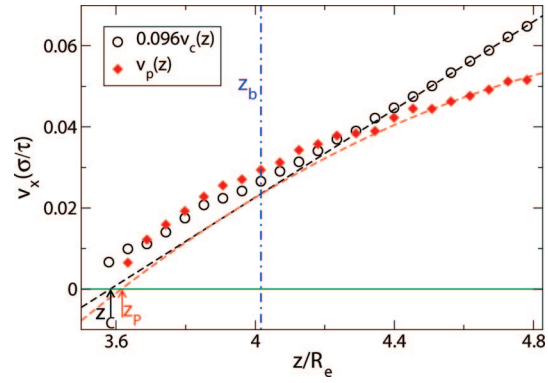

Figure 18. Velocity profiles and extrapolation of the fitted curves in the center region of the channel. Both Poiseuille (diamonds) and Couette (open circles) flows are shown for $\rho_g^* = 35.10$. The positions of z_P and z_C are indicated by arrows, and the hydrodynamic interface position, z_b, is marked by a vertical, dashed-dotted line.

the Navier−Stokes equation; the parameters depend not only on the brush but also on the type of flow. (iii) At very high grafting densities, the brush−melt interface becomes narrow, and the brush resembles an impenetrable elastic solid. In this case, we observe slip. Compared to the equilibrium wetting behavior, however, the grafting densities at which the crossover occur is shifted to higher values.

The brush−melt interface is a prototypical example of a soft, deformable substrate. We expect that similar behavior is found if the brush and melt chains were comprised of a different number of segments or if the segments were chemically different. Qualitatively, our findings are expected to carry over to interfaces between a polymer network and a melt. It has been suggested that the failure of the Navier slip condition is related to the increase of the viscosity at the surface. In fact, it has also been observed in polymer melts in contact with strongly attractive surfaces.[17] Other mechanisms, e.g., topographic surface structures or chain absorption, may also lead to similar effects, and we hope that our work stimulates the development of alternative boundary conditions for the Navier−Stokes equations that can consistently capture the properties of these soft surfaces.

Acknowledgment. We thank K. Ch. Daoulas, J. Servantie, and M. P. Allen for fruitful discussions. Financial support by the EU-INFLUS project NMP-031980, the Deutsche Forschungsgemeinschaft, project Mu 1674/3, SFB 625/A3, and a SECYT-DAAD collaboration grant is gratefully acknowledged. C.P. thanks ANPCYT for financial support (PICT 2005, PME 2006). Ample computing time has been provided by the Jülich Supercomputing center and GWDG, Göttingen.

References and Notes

(1) Tabelling, P. *Introduction to Microfluidics*; Oxford University Press: Oxford, 2006.
(2) Squires, T. M.; Quake, S. R. *Rev. Mod. Phys.* **2005**, *77*, 977.
(3) Navier, C. L. M. H. *Mem. Acad. Sci. Inst. Fr.* **1823**, *6*, 389.
(4) Young, T. *Philos. Trans. R. Soc. London* **1805**, *5*, 65.
(5) Grest, G. S.; Kremer, K. *Phys. Rev. A* **1986**, *33*, 3628.
(6) Klein, J.; Perahia, D.; Warburg, S. *Nature (London)* **1991**, *352*, 143.
(7) Grest, G. *Adv. Polym. Sci.* **1999**, *138*, 1.
(8) Doyle, P. S.; Shaqfeh, E. S. G.; Gast, A. P. *Macromolecules* **1998**, *31*, 5474.
(9) MacDowell, L. G.; Müller, M. *J. Chem. Phys.* **2006**, *124*, 084907.
(10) Dimitrov, D. I.; Milchev, A.; Binder, K. *Langmuir* **2008**, *24*, 1232.
(11) Pastorino, C.; Binder, K.; Kreer, T.; Müller, M. *J. Chem. Phys.* **2006**, *124*, 064902.
(12) Dimitrov, D. I.; Milchev, A.; Binder, K. *Phys. Rev. Lett.* **2007**, *99*, 054501.
(13) Priezjev, N. V.; Darhuber, A. A.; Troian, S. M. *Phys. Rev.* **2005**, *E 71*, 041608.

(14) Priezjev, N. V.; Troian, S. M. *Phys. Rev. Lett.* **2004**, *92*, 18302.
(15) Niavarani, A.; Priezjev, N. V. *Phys. Rev.* **2008**, *E 77*, 041606.
(16) Servantie, J.; Müller, M. *J. Chem. Phys.* **2008**, *128*, 014709.
(17) Servantie, J.; Müller, M. *Phys. Rev. Lett.* **2008**, *101*, 026101.
(18) Zhang, J.; Hansen, J. S.; Todd, B. D.; Daivis, P. J. *J. Chem. Phys.* **2007**, *126*, 144907.
(19) Varnik, F.; Binder, K. *J. Chem. Phys.* **2002**, *117*, 6336.
(20) Leibler, L.; Ajdari, A.; Mourran, A.; Coulon, G.; Chatenay, D. *Ordering in Macromolecular Systems, Proceedings of the Oums'93 Toyonaka, Osaka, Japan, 3−6 June 1993*; Springer-Verlag: Berlin, 1994.
(21) Matsen, M. W.; Gardiner, J. M. *J. Chem. Phys.* **2001**, *115*, 2794.
(22) Müller, M.; MacDowell, L. G. *Europhys. Lett.* **2001**, *55*, 221.
(23) Maas, J. H.; Fleer, G. J.; Leermakers, F. A. M.; Cohen-Stuart, M. *Langmuir* **2002**, *18*, 8871.
(24) Leermakers, F. A. M.; Maas, J. H.; Cohen-Stuart, M. *Phys. Rev.* **2002**, *E 66*, 051801.
(25) Müller, M.; MacDowell, L. G. *J. Phys.: Condens. Matter* **2003**, *15*, R609.
(26) MacDowell, L. G.; Müller, M. *J. Phys.: Condens. Matter* **2005**, *17*, S3523.
(27) Kerle, T.; Yerushalmi-Rosen, R.; Klein, J. *Macromolecules* **1998**, *31*, 422.
(28) Reiter, G.; Khanna, R. *Phys. Rev. Lett.* **2000**, *85*, 5599.
(29) Voronov, A.; Shafranska, O. *Langmuir* **2002**, *18*, 4471.
(30) Kröger, M. *Phys. Rep.* **2004**, *390*, 453.
(31) Baschnagel, J.; Varnik, F. *J. Phys.: Condens. Matter* **2005**, *17*, R851.
(32) Dünweg, B.; Kremer, K. *J. Chem. Phys.* **1993**, *99*, 6983.
(33) MacDowell, L. G.; Müller, M.; Vega, C.; Binder, K. *J. Chem. Phys.* **2000**, *113*, 419.
(34) Müller, M.; MacDowell, L. G. *Macromolecules* **2000**, *33*, 3902.
(35) MacDowell, L. G.; Müller, M.; Binder, K. *Colloids Surf., A* **2002**, *206*, 277.
(36) Müller, M.; MacDowell, L. G.; Yethiraj, A. *J. Chem. Phys.* **2003**, *118*, 2929.
(37) Hoogerbrugge, P. J.; Koelman, J. M. V. A. *Europhys. Lett.* **1992**, *19*, 155.
(38) Koelman, J. M. V. A.; Hoogerbrugge, P. J. *Europhys. Lett.* **1993**, *21*, 363.
(39) Espanol, P. *Phys. Rev. E* **1995**, *52*, 1734.
(40) Pastorino, C.; Kreer, T.; Müller, M.; Binder, K. *Phys. Rev.* **2007**, *E 76*, 026706.
(41) Smit, B.; Frenkel, D. *Understanding Molecular Simulation*, 2nd ed.; Academic Press: New York, 2002.
(42) Allen, M. P.; Tildesley, D. J. *Computer Simulation of Liquids*; Clarendon Press: Oxford, 1990.
(43) Buff, F. P.; Lovett, R. A.; Stillinger, F. H. *Phys. Rev. Lett.* **1965**, *15*, 621.
(44) Fredrickson, G. H.; Ajdari, A.; Leibler, L.; Carton, J. P. *Macromolecules* **1992**, *25*, 2882.
(45) Xi, H. W.; Milner, S. T. *Macromolecules* **1996**, *29*, 4772.
(46) Likhtman, A. E.; Anastasiadis, S. H.; Semenov, A. N. *Macromolecules* **1999**, *32*, 3474.
(47) Chacon, E.; Tarazona, P. *J. Phys.: Condens. Matter* **2005**, *17*, S3493.
(48) Werner, A.; Schmid, F.; Müller, M.; Binder, K. *Phys. Rev.* **1999**, *E 59*, 728.
(49) Mecke, K. R.; Dietrich, S. *Phys. Rev.* **1999**, *E 59*, 6766.
(50) Stecki, J. *J. Chem. Phys.* **2001**, *114*, 7574.
(51) Hiester, T.; Dietrich, S.; Mecke, K. *J. Chem. Phys.* **2006**, *125*, 184701.
(52) Vink, R. L. C.; Horbach, J.; Binder, K. *J. Chem. Phys.* **2005**, *122*, 134905.
(53) Chacon, E.; Tarazona, P.; Alejandre, J. *J. Chem. Phys.* **2006**, *125*, 014709.
(54) Tarazona, P.; Checa, R.; Chacon, E. *Phys. Rev. Lett.* **2007**, *99*, 196101.
(55) Blokhuis, E. M.; Kuipers, J.; Vink, R. L. C. *Phys. Rev. Lett.* **2008**, *101*, 086101.
(56) Müller, M.; Schick, M. *J. Chem. Phys.* **1996**, *105*, 8885.
(57) Werner, A.; Schmid, F.; Müller, M.; Binder, K. *J. Chem. Phys.* **1997**, *107*, 8175.
(58) Milchev, A.; Binder, K. *Europhys. Lett.* **2002**, *59*, 81.
(59) Müller, M.; Pastorino, C. *Europhys. Lett.* **2008**, *81*, 28002.
(60) Delgado-Buscalioni, R.; Chacon, E.; Tarazona, P. *Phys. Rev. Lett.* **2008**, *101*, 106102.
(61) Müller, M.; Macdowell, L. G. *Macromolecules* **2000**, *33*, 3902.
(62) Martini, A.; Hsu, H.; Patankar, N. A.; Lichter, S. *Phys. Rev. Lett.* **2008**, *100*, 206001.
(63) Dimitrov, D. I.; Milchev, A.; Binder, K. *Macromol. Theory Simul.* **2008**, *17*, 313.

MA8015757